Efficient Aeroelastic Beam Modelling and the Selection of a Structural Shape Basis

C. Howcroft[1], **S. A. Neild**[1], **M. H. Lowenberg**[1] **and J. E. Cooper**[1]
[1] Department of Aerospace Engineering, University of Bristol,
Queen's Building, University Walk, Bristol, BS34 7PA
e-mail: **c.howcroft@bristol.ac.uk**

Abstract

This paper considers the selection of structural shape bases for the modelling of flexible beams using the nonlinear beam shapes formulation. The approach provides a low order geometrically nonlinear representation of a flexible beam using a kinematic description that is geometrically exact; a minimal state representation is achieved by projecting the problem onto a set of shape functions spanning the beam. Motivated by the requirements for the low-order modelling of aeroelastic systems, this study examines the practical requirements of applying these shape sets to a flexible wing problem. A number of candidate shape sets are presented: orthogonal and non-orthogonal, with and without load dependent boundary conditions. The efficiency with which this problem is solved is used to assess the performance of each candidate shape set and infer the common properties between the most efficient bases. For a system with a moderate number of states a fairly consistent performance is observed across all of the sets. For larger sized problems, orthogonality of the shape basis is required to ensure robustness and scalability. It is shown that for a generic basis set the necessary boundary conditions of the problem can be easily satisfied, furthermore any orthogonal properties of a chosen basis can be retained. This concept is extended to allow for the treatment of more complex configurations starting from a simple shape basis.

Keywords: beam modelling, geometrically exact, reduced order, shape functions

1. Introduction

In the drive towards more efficient, long range aircraft configurations, high aspect ratio wing designs hold the potential to yield significant aerodynamic benefits; as well as principally reducing lift induced drag, the lower cruising speeds at which these designs are expected to operate also helps to mitigate wave drag effects (see aerodynamics texts such as [10]). However the same slender profiles that afford these benefits often result in structures that exhibit a high degree of flexibility. Consequently, large deformations are possible within the design loads envelope and thus geometric nonlinearities can play an important role in the observed response of the aircraft [13]. Such considerations are not only applicable to aircraft but also affect other slender aeroelastic structures such as wind turbine blades [11].

For systems such as these, a full picture of the dynamic behaviour not only relies on knowledge of the linear stability of the system in question, but on the full nonlinear dynamic characteristics. Examples in an aeroelastic context include [2, 3, 1] where Amabili et. al consider the large amplitude motion of cylindrical shells in supersonic flow, using numerical continuation to highlight the nonlinear characteristics of flutter beyond the linear stability boundary. In [7] Eaton et. al. treat a subsonic flexible wing, using continuation to show the existence of limit cycle oscillation below the linear theshold. Further examples of this type of subcritical phenomenon for high aspect ratio wings may also be observed in [12, 20]. Such results mean that in order to have confidence in the full range of dynamic behavior a system may exhibit, one must often simulate the entire system over large sets of test points. In this context there are obvious benefits to computationally efficient

analysis methods that can facilitate early trade-off and exploratory studies. Therefore, although a number of element-based structural codes have address the requirement for nonlinear modelling (e.g. absolute nodal coordinate [16], geometrically exact [17, 18], co-rotational [5, 4], intrinsic beam [8, 13], strain-based element [6, 19] to name but a few), this paper instead considers the nonlinear beam shapes formulation derived in [9] which uses global shape functions to significantly reduce the number of states over which the geometrically nonlinear problem is expressed. The choice of a suitable admissible shape set is central to realising this efficient representation. This study aims to identify desired characteristics and boundary properties of these shape sets and thus help formalise their generation and application to the nonlinear beam shapes problem.

The paper is organised as follows. In section 2, a summary of the nonlinear beam shapes formulation is provided. Section 3 introduces the shape sets to be used in the study and discusses the use of scaling to satisfy additional boundary requirements. Section 4 describes the aeroelastic test case treated in this study as well as the convergence criterion that will be used to quantify the accuracy of its solution. This criterion is applied in section 5 to assess the performance of the candidate shape sets, and comments are made as to the satisfaction of natural boundary conditions and orthogonality. In section 6 the findings of the previous sections are used to infer the treatment of discontinuous geometries; general conclusions of the entire study are outlined in section 7.

2. Overview of Nonlinear Beam Shapes Method

The work of this study is based around the nonlinear beam shapes formulation detailed in [9], allowing for the treatment of a geometric (and materially) nonlinear beam structure using a small set of describing states. The formulation is constructed using a global referenced attitude parameterisation of a body fixed local coordinate system; this coordinate system follows the deforming structure at each spanwise location along the beam. This concept is demonstrated by the deflected beam depicted in figure 1, also taken from reference [9]. The vector $\boldsymbol{\Gamma}(s)$ is used to denote the beam reference line in the global (X, Y, Z) system, where s is the curvilinear spanwise coordinate. The intrinsic/local reference frame is given by the three vectors $\boldsymbol{e}_x(s)$, $\boldsymbol{e}_y(s)$ and $\boldsymbol{e}_z(s)$ and is displayed in the figure at an example spanwise location. The chosen attitude parameterisation mapping the orientation of this local triad to the coordinate system $[A]$ takes the form of a 3-1-2 Euler angles parameterisation in the angular variables ψ-θ-ϕ, respectively. Thus one may write

$$\begin{aligned}\mathbf{e}_{[A]} &= \left(\boldsymbol{e}_{x[A]} \mid \boldsymbol{e}_{y[A]} \mid \boldsymbol{e}_{z[A]}\right) = \boldsymbol{R}_E \left(\boldsymbol{x}_E \mid \boldsymbol{y}_E \mid \boldsymbol{z}_E\right) \boldsymbol{R}_{\boldsymbol{E}}^{\boldsymbol{T}} \\ &= \boldsymbol{R}_E \begin{pmatrix} c_s\,\psi c_s\,\phi + s_n\theta s_n\psi s_n\phi & c_s\,\theta s_n\psi & c_s\,\psi s_n\phi - s_n\theta s_n\psi c_s\,\phi \\ -s_n\psi c_s\,\phi + s_n\theta c_s\,\psi s_n\phi & c_s\,\theta c_s\,\psi & -s_n\psi s_n\phi - s_n\theta c_s\,\psi c_s\,\phi \\ -c_s\,\theta s_n\phi & s_n\theta & c_s\,\theta c_s\,\phi \end{pmatrix} \boldsymbol{R}_{\boldsymbol{E}}^{\boldsymbol{T}}\,, \end{aligned} \tag{1}$$

where s_n and c_s are used as shorthand notation for the trigonometric operations 'sin()' and 'cos()'. $\boldsymbol{R}_E$ is an optional transform allowing one to place the $\theta = \pm 90\,\text{deg}$ Euler singularities at any orientation in the coordinate system $[A]$; throughout this study $\boldsymbol{R}_E$ is assigned the 3×3 identity matrix. Given this parameterisation the beam reference line is recovered via spanwise integration with respect to this vector triad. In the absence of shear and extensional strain (see [9] for details of these terms) $\boldsymbol{\Gamma}_{[A]}$ may be written as

$$\boldsymbol{\Gamma}_{[A]}(s) = \int_0^s \boldsymbol{e}_{y[A]}(\tilde{s})\,\mathrm{d}\tilde{s} \tag{2}$$

The equations of motion for this flexible structure will be formed by considering a series of virtual work contributions following incremental deflections ($\boldsymbol{\delta\Gamma}$), rotations ($\boldsymbol{\delta\vartheta}$) and strains ($\boldsymbol{\delta\kappa}$) realised along the length of the flexible beam. Expressions for these variations may be written,

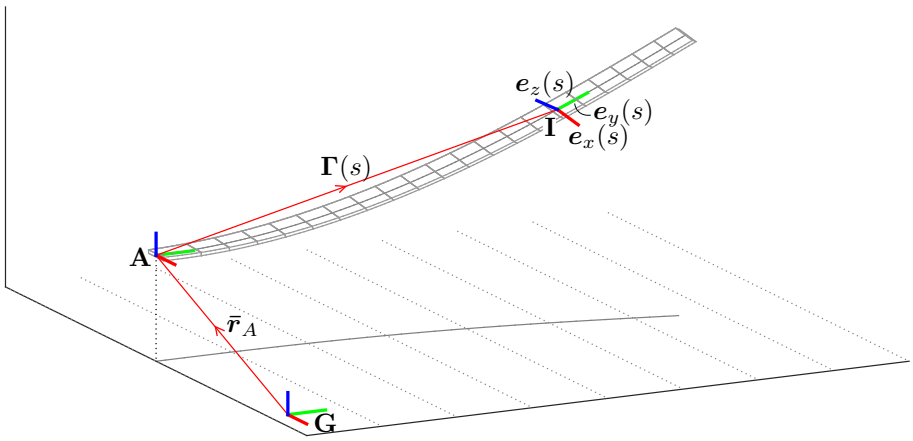

Figure 1: Positional vectors and coordinate systems used in expressing the deflected beam geometry; taken from [9].

$$\boldsymbol{\delta\Gamma}_{[A]}(s) = \int_0^s \boldsymbol{\delta e}_{y[A]}(\tilde{s})\,\mathrm{d}\tilde{s} \tag{3}$$

$$\boldsymbol{\delta\vartheta}_{[A]}(s) = \frac{1}{2}(\boldsymbol{e}_{x[A]} \times \boldsymbol{\delta e}_{x[A]} + \boldsymbol{e}_{y[A]} \times \boldsymbol{\delta e}_{y[A]} + \boldsymbol{e}_{z[A]} \times \boldsymbol{\delta e}_{z[A]}) \tag{4}$$

$$\boldsymbol{\delta\kappa}_{[I]}(s) = (\delta\kappa_x\,,\,\delta\kappa_y\,,\,\delta\kappa_z)^T = \left(\delta[\boldsymbol{e'}_{y[A]} \cdot \boldsymbol{e}_{z[A]}]\,,\,\delta[\boldsymbol{e'}_{z[A]} \cdot \boldsymbol{e}_{x[A]}]\,,\,\delta[\boldsymbol{e'}_{x[A]} \cdot \boldsymbol{e}_{y[A]}]\right)^T \tag{5}$$

Note that since the test cases treated in this study comprise wings that are clamped at the root, the coordinate systems $[A]$ and $[G]$ from figure 1 are taken to be coincident, with $\bar{\boldsymbol{r}}_A = \boldsymbol{0}$. Thus in this summary $[A]$ constitutes an inertial reference frame. Given the variations (3)–(5), the incremental work terms may be categorised by the following expressions:

$$\text{Applied Force} \qquad \delta W_F = \int_0^L \boldsymbol{F}_{[A]} \cdot \boldsymbol{\delta\Gamma}_{[A]}\,\mathrm{d}s \tag{6}$$

$$\text{Applied Moment} \qquad \delta W_M = \int_0^L \boldsymbol{M}_{[A]} \cdot \boldsymbol{\delta\vartheta}_{[A]}\,\mathrm{d}s \tag{7}$$

$$\text{Stiffness} \qquad \delta W_K = \int_0^L \boldsymbol{F}_{K[I]}(\boldsymbol{\Delta\kappa}_{[I]}) \cdot \boldsymbol{\delta\kappa}_{[I]}\,\mathrm{d}s \tag{8}$$

$$\text{Damping} \qquad \delta W_C = \int_0^L \boldsymbol{F}_{C[I]}(\boldsymbol{\Delta\kappa}_{[I]}, \dot{\boldsymbol{\kappa}}_{[I]}) \cdot \boldsymbol{\delta\kappa}_{[I]}\,\mathrm{d}s \tag{9}$$

$$\text{Linear Momentum} \qquad \delta W_{TL} = \int_0^L -\frac{\mathrm{d}}{\mathrm{d}t}\left(m\dot{\boldsymbol{\Gamma}}_{[A]}\right) \cdot \boldsymbol{\delta\Gamma}_{[A]}\,\mathrm{d}s \tag{10}$$

$$\text{Angular Momentum} \qquad \delta W_{TR} = \int_0^L -\frac{\mathrm{d}}{\mathrm{d}t}\left(\mathbf{e}_{[A]}\boldsymbol{I}_{\vartheta[I]}\mathbf{e}^{\boldsymbol{T}}_{[\boldsymbol{A}]}\dot{\boldsymbol{\vartheta}}_{[A]}\right) \cdot \boldsymbol{\delta\vartheta}_{[A]}\,\mathrm{d}s \tag{11}$$

Where $\boldsymbol{F}_{[A]}$ and $\boldsymbol{M}_{[A]}$ are force and moment distributions acting along the beam reference line. $\boldsymbol{\Delta\kappa}_{[I]} = \boldsymbol{\kappa}_{[I]} - \boldsymbol{\kappa}_0$ where $\boldsymbol{\kappa}_0$ is the initial curvature of the beam; $\boldsymbol{F}_{K[I]}$ is the constitutive law relating local internal stresses to this curvature; $\boldsymbol{F}_{C[I]}$ is the assumed damping law which may depend on both the rate and absolute value of the curvature. m is the mass per unit length of the beam and $\boldsymbol{I}_{\vartheta[I]}$ is the inertia per span matrix in the local coordinate system, expressed about the beam reference line; note that the cross sectional centre of mass is assumed to lie along $\boldsymbol{\Gamma}_{[A]}$ in these expressions. From d'Alembert's principle the net virtual work variation δW over all of these

contributions will be zero:

$$\delta W_F + \delta W_M + \delta W_K + \delta W_C + \delta W_{TL} + \delta W_{TR} = \delta \mathrm{W}(\,\theta(s,t), \psi(s,t), \phi(s,t)\,) = 0 \tag{12}$$

A governing set of equations describing the behaviour of this system may be produced by relating this variational net virtual work to a system of generalised coordinates $\boldsymbol{q}$. This formulation is achieved via a shape based decomposition of each of the spanwise $\phi(s)$, $\psi(s)$ and $\theta(s)$ Euler parameters as a linear combination of suitable shape functions; the specific weighting of these functions relating to the elements of the vector $\boldsymbol{q} = [\boldsymbol{q}_\theta, \boldsymbol{q}_\psi, \boldsymbol{q}_\phi]^T$ such that

$$\theta(s) = \sum_i \Theta_i(s) q_{\theta i}\ , \quad \psi(s) = \sum_j \Psi_j(s) q_{\psi j}\ , \quad \phi(s) = \sum_k \Phi_k(s) q_{\phi k} \tag{13}$$

By taking the partial derivatives of (12) with respect to each of the generalised coordinates $q_n \in \boldsymbol{q}$ one obtains

$$\frac{\partial W_F}{\partial q_n} + \frac{\partial W_M}{\partial q_n} + \frac{\partial W_K}{\partial q_n} + \frac{\partial W_C}{\partial q_n} + \frac{\partial W_{TL}}{\partial q_n} + \frac{\partial W_{TR}}{\partial q_n} = \frac{\partial}{\partial q_n} \mathrm{W}(\,\theta(s,t), \psi(s,t), \phi(s,t)\,) = 0\ . \tag{14}$$

Substituting in (6)–(11) and using the linear stiffness and damping models

$$\boldsymbol{F}_{K[I]} = -\bar{\boldsymbol{K}}\boldsymbol{\kappa} \qquad\qquad \boldsymbol{F}_{C[I]} = -\bar{\boldsymbol{C}}\dot{\boldsymbol{\kappa}} \tag{15}$$

yields

$$\begin{aligned}\int_0^L \Bigg(\boldsymbol{F}_{[A]} \cdot \frac{\partial \boldsymbol{\Gamma}_{[A]}}{\partial q_n} + \boldsymbol{M}_{[A]} \cdot \frac{\partial \boldsymbol{\vartheta}_{[A]}}{\partial q_n} - (\bar{\boldsymbol{K}}\boldsymbol{\kappa}) \cdot \frac{\partial \boldsymbol{\kappa}_{[I]}}{\partial q_n} - (\bar{\boldsymbol{C}}\dot{\boldsymbol{\kappa}}) \cdot \frac{\partial \boldsymbol{\kappa}_{[I]}}{\partial q_n} \\ - \frac{\mathrm{d}}{\mathrm{d}t}\left(m\dot{\boldsymbol{\Gamma}}_{[A]}\right) \cdot \frac{\partial \boldsymbol{\Gamma}_{[A]}}{\partial q_n} - \frac{\mathrm{d}}{\mathrm{d}t}\left(\mathbf{e}_{[A]} \boldsymbol{I}_{\vartheta[I]} \mathbf{e}_{[A]}^{\boldsymbol{T}} \dot{\boldsymbol{\vartheta}}_{[A]}\right) \cdot \frac{\partial \boldsymbol{\vartheta}_{[A]}}{\partial q_n} \Bigg)\ \mathrm{d}s = 0\end{aligned} \tag{16}$$

This system of equations prescribes the full dynamics of the flexible beam and may be recast into the convenient matrix form:

$$\boldsymbol{M}(\dot{\boldsymbol{q}}, \boldsymbol{q})\ \ddot{\boldsymbol{q}} = \boldsymbol{f}(\dot{\boldsymbol{q}}, \boldsymbol{q}) \tag{17}$$

see [9] for the in-depth formulation of this dynamic system.

For much of the work of this study, the focus will be on the static form of these equations, i.e.

$$\int_0^L \left(-(\bar{\boldsymbol{K}}\boldsymbol{\kappa}) \cdot \frac{\partial \boldsymbol{\kappa}_{[I]}}{\partial q_n} + \boldsymbol{M}_{[A]} \cdot \frac{\partial \boldsymbol{\vartheta}_{[A]}}{\partial q_n} + \boldsymbol{F}_{[A]} \cdot \frac{\partial \boldsymbol{\Gamma}_{[A]}}{\partial q_n} \right)\ \mathrm{d}s = 0 \tag{18}$$

This algebraic system may be written in the shorthand form

$$\mathbf{W}_q(\boldsymbol{q}(t), \boldsymbol{\Theta}(s), \boldsymbol{\Psi}(s), \boldsymbol{\Phi}(s)) = \mathbf{0} \tag{19}$$

the exact form of which is dependent on the chosen shape sets $\boldsymbol{\Theta}(s)$, $\boldsymbol{\Psi}(s)$ and $\boldsymbol{\Phi}(s)$.

3. Shape Function Sets

In applying the above formulation to the modelling of a flexible beam problem, one must specify a suitable set of shape functions onto which the problem is projected. Depending on the particular

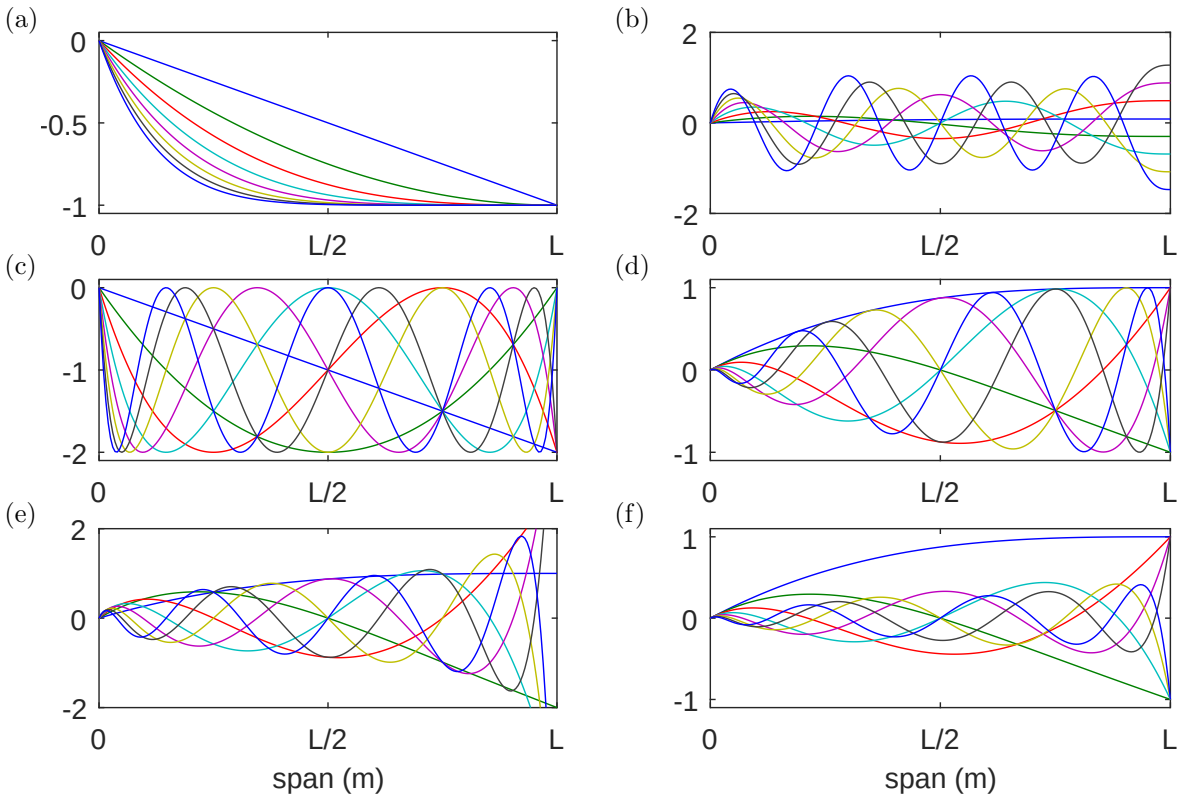

Figure 2: Depiction of the first eight shapes for each example set type used in this study. The panels (a)–(f) correspond to the indicated entries in table 1.

configuration of the problem being modelled there may be additional kinematic constraints; these may be either directly satisfied by the shape functions used or, alternatively, extra penalty functions may be introduced to effectively enforce these constraints through minimisation of the variational problem. In the examples of this study a clamped root condition is employed. The root tangency condition imposes a maximal number of root constraints on the shape sets approximating the three kinematic parameters and thus forms a suitable exercising test condition[1]. Specifically, this dictates the root constraint

$$\Theta(0) = \Psi(0) = \Phi(0) = 0 \tag{20}$$

Six shape function sets satisfying this condition are considered for this study. These sets are presented in table 1; for each set, generating expressions are given along with an indication as to whether the set is orthogonal (if so, the corresponding weighting function is also provided). A depiction of the first eight shapes of each of these sets is also provided in the panels of figure 2.

Note that the 4th, 5th and 6th sets in table 1 are referred to as modified sets. This is due to the use of the scaling functions $E(s)$ and $x(s)$ that are used in conjunction with the standard Chebyshev/Legendre definitions. The reasons for these scaling functions are twofold. Firstly, by choosing $E(s)$ such that $E(0) = 0$ one immediately ensures that the kinematic condition (20) is satisfied. Secondly, via selection of both $E(s)$ and $x(s)$ one may also warp these shape sets in such a way as to satisfy additional derivative boundary conditions (with respect to 's') at specific spanwise locations. This scaling transform is depicted in figure 3 for a set of Chebyshev polynomials of the first kind. In panel (a) the unaltered set is depicted, linearly mapped onto the interval $L \in [0, s]$ (and technically reversed). In panel (b) the E(s) scaling function is applied to these functions to bring the left hand values to zero. In panel (c) the mapping $x \in [-1, 1] \rightarrow s \in [O, L]$ is altered so

[1]The zero displacement condition at the root is implicitly satisfied by equation (2).

Set Name	Figure	Generating Functions, $y_n(s)$	Orthogonal	Weight Function, $W(s)$
Reverse Polynomial	2(a)	$x = s/L$ $y_n(s) = (1-x)^n$	No	—
Mode Shapes	2(b)	$y_n(s) = \frac{\mathrm{d}}{\mathrm{d}s}[\Phi_n(s)]$ where $\Phi_n(x)$ is the standard set of n cantilever mode shapes.	No	—
Shifted Chebyshev 1st	2(c)	$x = -2(s/L) + 1$ $T_1 = 1$ $T_2 = x$ $T_n = 2xT_{n-1}(x) - T_{n-2}(x)$ $y_n(s) = T_n(x(s)) - 1$	No	—
Modified Chebyshev 1st	2(d)	$T_n = ..$ *as above* $..$ $y_n(s) = E(s)T_n(x(s))$ where $E = (s/L)^3 - 3(s/L)^2 + 3(s/L)$	Yes	$E^{-2}(s)x'(s)(1-x^2)^{-1/2}$
Modified Chebyshev 2nd	2(e)	$x = -2(s/L) + 1$ $U_1 = 1$ $U_2 = 2x$ $U_n = 2xU_{n-1}(x) - U_{n-2}(x)$ $y_n(s) = E(s)U_n(x(s))$ where $E = (s/L)^3 - 3(s/L)^2 + 3(s/L)$	Yes	$E^{-2}(s)x'(s)(1-x^2)^{1/2}$
Modified Legendre	2(f)	$x = -2(s/L) + 1$ $P_1 = 1$ $P_2 = x$ $P_n = \frac{(2n-3)xP_{n-1} - (n-2)P_{n-2}}{(n-1)}$ $y_n(s) = E(s)P_n(x(s))$ where $E(s) = (s/L)^3 - 3(s/L)^2 + 3(s/L)$	Yes	$E^{-2}(s)x'(s)$

Table 1: The candidate shape sets used throughout this study.

as to bring the derivative dy/ds to zero at the right hand limit. It is this method of scaling that is later used in this study to satisfy the load dependent boundary conditions detailed in section 4.3.

3.1. Shape Set Scaling

It is important to note that orthogonality of the modified shape sets may be retained following the application of the E(s) and x(s) scaling functions. To illustrate this point consider the standard definition of orthogonality as applied to a generic shape set y_i spanning the x domain ($x \in [x_0, x_1]$).

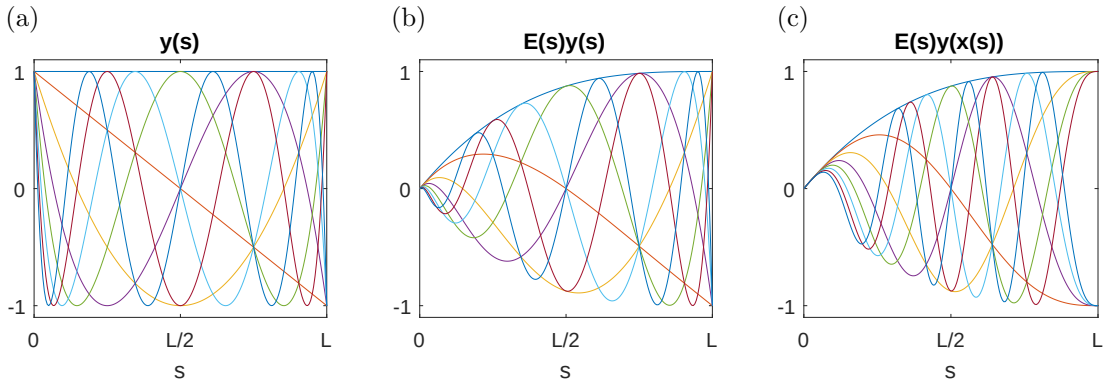

Figure 3: Scaling of the Chebyshev polynomial base set (a) to satisfy the zero kinematic constraint (b) and zero tip derivative conditions (c).

$$\langle y_i, y_j \rangle = \int_{x_0}^{x_1} y_i(x) y_j(x) W(x)\, \mathrm{d}x = \begin{cases} 0 & i \neq j \\ \|y_i\|^2 & i = j \end{cases} \tag{21}$$

$W(x)$ is the positive definite weighting function for the orthogonal set $y(x)$, i.e. $W(x) \in \Re^+ \ \forall x \in [x_1, x_2]$. Applying the $E(s)$ and $x(s)$ scaling to this definition such that $y(x) \to E(s)y(x(s))$ and collecting terms yields:

$$\int_{x_0}^{x_1} y_i(x) y_j(x) W(x)\, \mathrm{d}x = \int_{s_0}^{s_1} \Big(E(s) y_i(x(s)) \Big) \Big(E(s) y_j(x(s)) \Big) \left(\frac{W(x(s))}{E(s)^2} \frac{\mathrm{d}x}{\mathrm{d}s} \right) \mathrm{d}s \tag{22}$$

Thus, providing the quantity $W(x(s))E(s)^{-2}x'(s)$ also constitutes a positive definite function over the domain $s \in [s_0, s_L]$, orthogonality of the scaled set $E(s)y(x(s))$ is retained. This result is very useful in practise as it allows one to choose from a largely arbitrary set of shape bases when setting up a problem with the knowledge that the essential kinematic conditions (and additional load constraints) of the problem may be trivially satisfied via scaling — all whilst maintaining any orthogonal properties of the set. This greatly simplifies the process of applying the nonlinear beam shapes formulation to a generic beam-like problem.

4. Test Case

4.1. Wing Model

As discussed in the introduction, the nonlinear beam shapes formulation will be applied in this study to the modelling of a slender aircraft wing, from which discussions as to its efficient application will be drawn. The aeroelastic system in question will consist of the rectangular half wing based on the high aspect ratio aircraft of Patil et al [13]. This half-wing has a rectangular planform with an aspect ratio of 16. Aerodynamic cross sections along the span of the wing comprise NACA0012 profiles. The parameters pertinent to the definition of this wing are detailed in table 2.

For the aerodynamic modelling a quasi steady vortex lattice representation is selected. Since aerodynamic fidelity is not a primary concern here, a discretisation of 20 equal-width horseshoe vortices is used. This coarse distribution is sufficient to qualitatively represent the spanwise aerodynamic loading without dominating the computation effort required for solution of the aeroelastic test case. The resultant force $F_{[A]}(s)$ and moment $M_{[A]}(s)$ distributions calculated from this model are applied directly to the beam reference line $\mathbf{\Gamma}(s)$ — see equations (6) and (7).

Wing Properties	Value	Units
Geometric		
Semi-span	16	m
Chord	1	m
Taper ratio	1	-
1/4 chord sweep	0	deg
Dihedral	0	deg
Structural		
Mass per unit length	0.75	kg/m
In-Plane Bending Stiffness, EI_{xx}	2×10^4	Nm^2
Out-of-Plane Bending Stiffness, EI_{zz}	4×10^6	Nm^2
Torsional Stiffness, GJ	1×10^4	Nm/rad

Table 2: Geometric and structural properties of the wing model.

4.2. Load Cases

For the initial analysis, four test cases will be considered, each representing a different loading of the clamped half wing. Each of these is depicted in figure 4. Panels (a) and (b) comprise tip loading test cases and panels (c) and (d), distributed load cases. Furthermore, the cases depicted in panels (a) and (c) act to produce a purely planar deformation of the wing, whereas those of panels (b) and (d) deform the wing in three dimensions. These four load cases therefore represent a good variety of loading characteristics. The definition of each applied load is given in table 3. Note that the root angle of attack for the 1g trim case has been calculated from a single simulation using 60 shape functions and is kept constant throughout the entire study (hence the wing will not be re-trimmed for each shape set).

Test Case	Figure	Load Definition
Tip Follower	4(a)	$\boldsymbol{F}_{[A]}(s) = 200\,\delta(s-L)\boldsymbol{e}_{z[A]}(L) \quad N$
Tip Global	4(b)	$\boldsymbol{F}_{[A]}(s) = \delta(s-L)(200, 0, 200) \quad N$
Self Weight	4(c)	–
1g Trim	4(d)	$\alpha = 5.6^{\circ}$ **Flight condition** Airspeed = 30 m/s Air density = 0.0881 kg/m^3 Mach No. = 0.1017 Altitude = 20000 ft

Table 3: Flight condition used for the aeroelastic test case. For the tip load cases, δ denotes the Dirac delta function.

4.3. Natural Boundary Conditions

For each of the four load cases detailed above, additional natural boundary conditions may be applied to reflect the tip shear and moment characteristics of each load case. These boundary forces and moments map via the Euler Bernoulli constitutive material law to a set of conditions on $\theta(L)$, $\psi(L)$ and $\phi(L)$. For this study the following additional natural load condition are considered for each load case:

$$\begin{aligned}
\text{TipFollower}: &\quad \theta'(L), \psi'(L), \phi'(L) = 0 &\quad \theta''(L), \psi''(L), \phi''(L) \neq 0 \\
\text{TipGlobal}: &\quad \theta'(L), \psi'(L), \phi'(L) = 0 &\quad \theta''(L), \psi''(L), \phi''(L) \neq 0 \\
\text{SelfWeight}: &\quad \theta'(L), \psi'(L), \phi'(L) = 0 &\quad \theta''(L), \psi''(L), \phi''(L) = 0 \\
\text{1gTrim}: &\quad \theta'(L), \psi'(L), \phi'(L) = 0 &\quad \theta''(L), \psi''(L), \phi''(L) \neq 0
\end{aligned} \tag{23}$$

The constraints $\theta'(L), \psi'(L), \phi'(L) = 0$ ensure zero curvature at the tip and thus represent a zero tip moment; this applies to all of the load cases. Non-zero $\theta''(L)$, $\psi''(L)$ and $\phi''(L)$ values allow

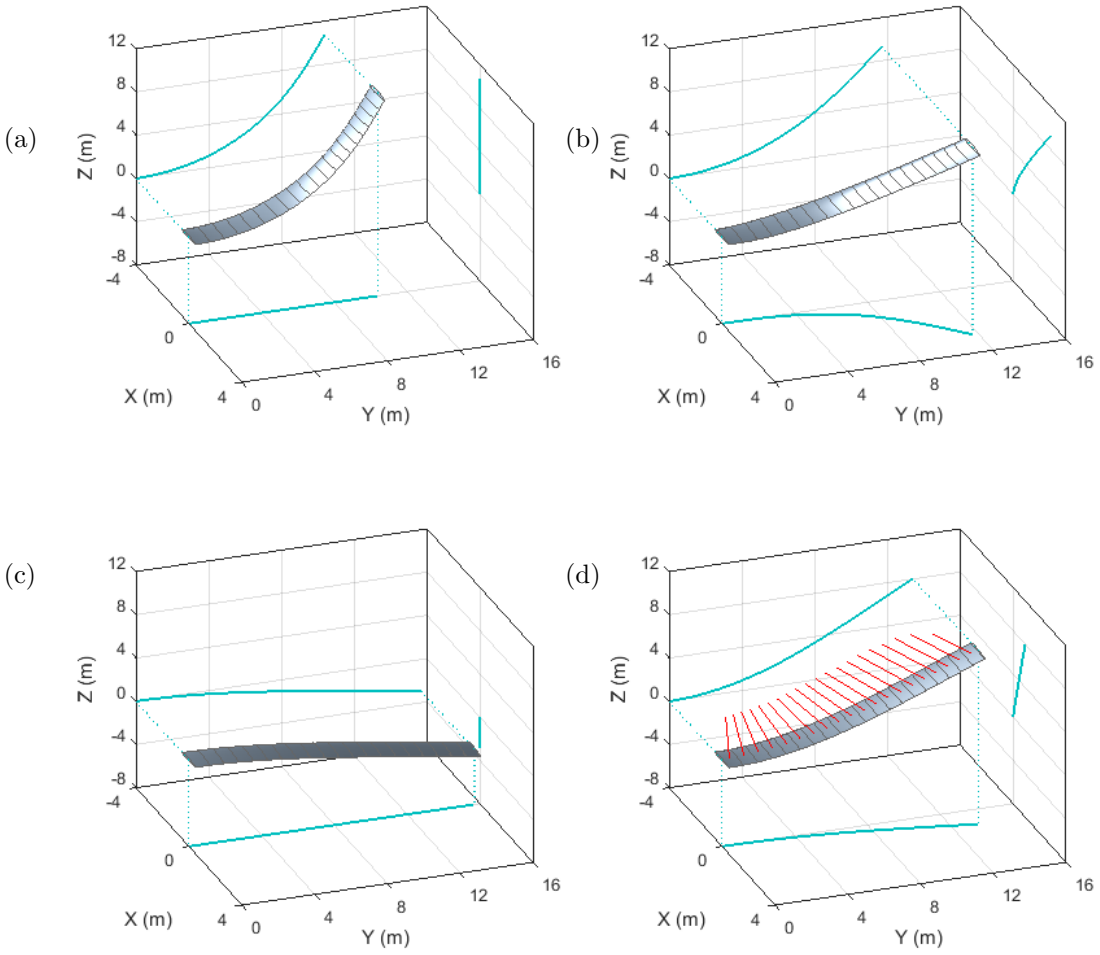

Figure 4: The four load cases applied to the Patil-Hodges wing and the resulting structural deformations. Panels depict the (a) tip follower, (b) tip global, (c) self weight and (d) 1g trim loads.

for tip shear loads; this condition applies to the two tip load test cases. Note however that these second derivatives are also afforded a non-zero value for the 1g Trim case. This is because, despite a zero applied tip shear for the 1g Trim case, a better performance is observed by relaxing the zero second derivative constraints in the solution of the static problem. These four conditions will be used later in this study to assess the benefits in satisfying additional load dependent boundary conditions.

4.4. Convergence Criterion

To assess the physical accuracy of any obtained static deformations of the Patil-Hodges wing, a suitable convergence criterion is first defined. Beginning with the constitutive law of the system (15) and rearranging yields

$$\bar{\boldsymbol{K}}^{-1}(s)\boldsymbol{F}_{K[I]}(s) + \boldsymbol{\kappa}(s) = 0\,. \tag{24}$$

Recall that $\boldsymbol{F}_{K[I]}(s)$ is a generalised internal load vector, in this case equal to the distributed internal moment. This force quantity may also be estimated based on the loads applied to the

system and knowledge of the beam geometry. Specifically one may write

$$\boldsymbol{F}^{*}_{K[I]}(s) = -\boldsymbol{e}^{T}_{[A]} \int_{s}^{L} (\boldsymbol{\Gamma}_{[A]}(\tilde{s}) - \boldsymbol{\Gamma}_{[A]}(s)) \times \boldsymbol{F}_{[A]}(\tilde{s}) + \boldsymbol{M}_{[A]}(\tilde{s})\, \mathrm{d}\tilde{s} \tag{25}$$

where $\boldsymbol{F}_{[A]}(s)$ and $\boldsymbol{M}_{[A]}(s)$ are taken to include the effects of self weight in addition to the directly applied loads. When the system has achieved static equilibrium

$$\boldsymbol{F}^{*}_{K[I]}(s) = \boldsymbol{F}_{K[I]}(s) \qquad \forall s \in [0, L] \tag{26}$$

Substituting this internal load estimate into equation (24) one may define the 3×1 convergence vector $\boldsymbol{C}_{\nu}$ with components in each of the three intrinsic $\boldsymbol{e}_x$, $\boldsymbol{e}_y$, $\boldsymbol{e}_z$ directions, such that

$$\int_{0}^{L} (\, \bar{\boldsymbol{K}}^{-1}(s) \boldsymbol{F}^{*}_{K[I]}(s) + \boldsymbol{\kappa}(s)\,)^2 \, \mathrm{d}s = \boldsymbol{C}_{\nu} \quad , \qquad\qquad c_{\nu} = \sum_{i} \boldsymbol{C}_{\nu\, i} \tag{27}$$

where $\boldsymbol{C}_{\nu} \to \boldsymbol{0}$ as one approaches the static solution. The single scalar convergence measure c_{ν} is also defined, equal to the sum of the components of $\boldsymbol{C}_{\nu}$.

An illustration of this convergence is provided in figure 5 for the global tip load case. The solid and dashed curves shown in the plots relate to the two components of equation (27), indicated in the legend; the closer these two curves are in each plot, the better the convergence. Panels (a)–(c) show this comparison for each of the three components of $\boldsymbol{C}_{\nu}$ using eight Chebyshev 1st polynomials — (2,3,3) indicates the number of functions used for the θ, ψ and ϕ Euler angles respectively. Each $\boldsymbol{C}_{\nu}$ component value is written above the relevant panel; overall a scalar sum of $c_{\nu} = 1.332 \times 10^{-3}$ is achieved. Panels (d)–(f) repeat this test using seventeen shape functions (7,5,5). The better convergence can be directly observed from these latter three plots and an improved convergence measure $c_{\nu} = 1.262 \times 10^{-6}$ is achieved.

This convergence measure is used throughout the remainder of the study. The advantage of this approach is that one may directly assess convergence without needing to track incremental changes in the solution over a sequence of iterations. Furthermore, the fact that the vector $\boldsymbol{C}_{\nu}$ comprises three components in the intrinsic $\boldsymbol{e}_x$, $\boldsymbol{e}_y$ and $\boldsymbol{e}_z$ directions provides clues as to which Euler parameter the next shape should be added to best improve convergence.

5. Convergence Tests

A series of results are now presented, showing the number of shapes required in meeting the convergence threshold $c_{\nu} < 1 \times 10^{-6}$. This value is deemed sufficient to ensure that the deformation of the wing for each of the previously defined load cases is accurately captured. For example, in moving from $c_{\nu} = 1 \times 10^{-6} \to 1 \times 10^{-7}$ the tip deformation for the global tip load case changes by only 0.25 mm.

Table 4 shows the results of this convergence study; each column of data corresponds to one of the four load cases; the rows correlate with each of the considered shape sets. For each data entry the first number refers to the total number of shapes required in meeting the convergence criterion; the trio of values in brackets provides the breakdown of these shapes into the θ, ψ and ϕ Euler parameters, respectively. The value after the brackets indicates the number of function evaluations required in solving the static problem; this latter value serves as a rough indication as to the computational effort required in treating the corresponding load/shape-set case. In all cases the static solution is achieved using the MATLAB 'fsolve' optimisation routine based on the Powell Dogleg algorithm [14].

Looking across the four load cases one immediately notes that the tip global and 1g trim tests require the largest shape sets in meeting the convergence criterion; indeed, since both of these

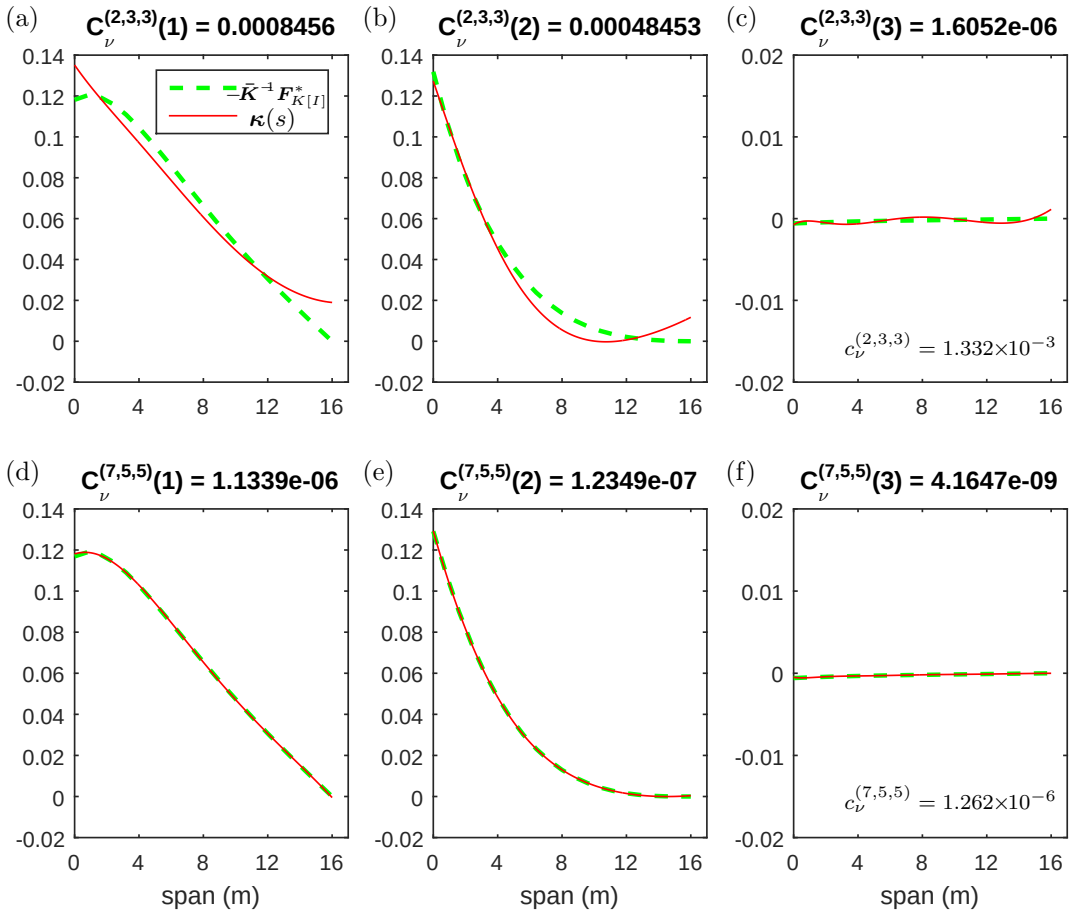

Figure 5: A depiction of the convergence criterion for the tip global load case. Panels (a)–(c) correspond to an eight shape function approximation; panels (d)–(f) to a seventeen shape approximation.

EntryFormat : nShapes $(n\theta\ n\psi\ n\phi)$, functionCalls	Tip Follower	Tip Global	Self Weight	1g Trim
Reverse polynomial, BCs: not matched	4 (4 0 0), 35	18 (6 7 5), 1126	3 (3 0 0), 30	15 (5 6 4), 214
Reverse polynomial, BCs: matched	3 (3 0 0), 30	15 (5 5 5), 467	2 (2 0 0), 25	12 (4 5 3), 199
Mode shapes	—	—	3 (3 0 0), 30	10 (2 4 4), 221
Chebyshev 1st (E), BCs: not matched	5 (5 0 0), 40	18 (8 5 5), 401	2 (2 0 0), 25	13 (4 5 4), 228
Chebyshev 1st (E), BCs: matched	2 (2 0 0), 25	15 (5 5 5), 677	2 (2 0 0), 20	13 (5 5 3), 199
Chebyshev 2nd (E), BCs: not matched	5 (5 0 0), 40	18 (8 5 5), 555	2 (2 0 0), 25	13 (4 5 4), 199
Chebyshev 2nd (E), BCs: matched	2 (2 0 0), 25	15 (5 5 5), 708	2 (2 0 0), 25	13 (5 5 3), 326
Legendre (E), BCs: not matched	5 (5 0 0), 40	18 (8 5 5), 401	2 (2 0 0), 25	13 (4 5 4), 228
Legendre (E), BCs: matched	2 (2 0 0), 25	15 (5 5 5), 708	2 (2 0 0), 20	13 (5 5 3), 228
Chebyshev – 1, BCs: not matched	4 (4 0 0), 35	18 (6 7 5), 688	3 (3 0 0), 30	15 (5 6 4), 179
Chebyshev – 1, BCs: matched	2 (2 0 0), 25	15 (5 5 5), 387	2 (2 0 0), 25	13 (5 5 3), 157

Table 4: Table showing the number of shape functions required by each of the candidate shape sets in meeting the convergence criterion $c_\nu < 1 \times 10^{-6}$.

load cases act to produce a deformation of the wing in all three cardinal dimensions, this is to be expected when compared to the planar deflection cases. The larger state size of the tip global and 1g trim cases is accompanied by a correspondingly high number of required function evaluations in reaching a solution. Regarding the properties and observed performance of the candidate shape

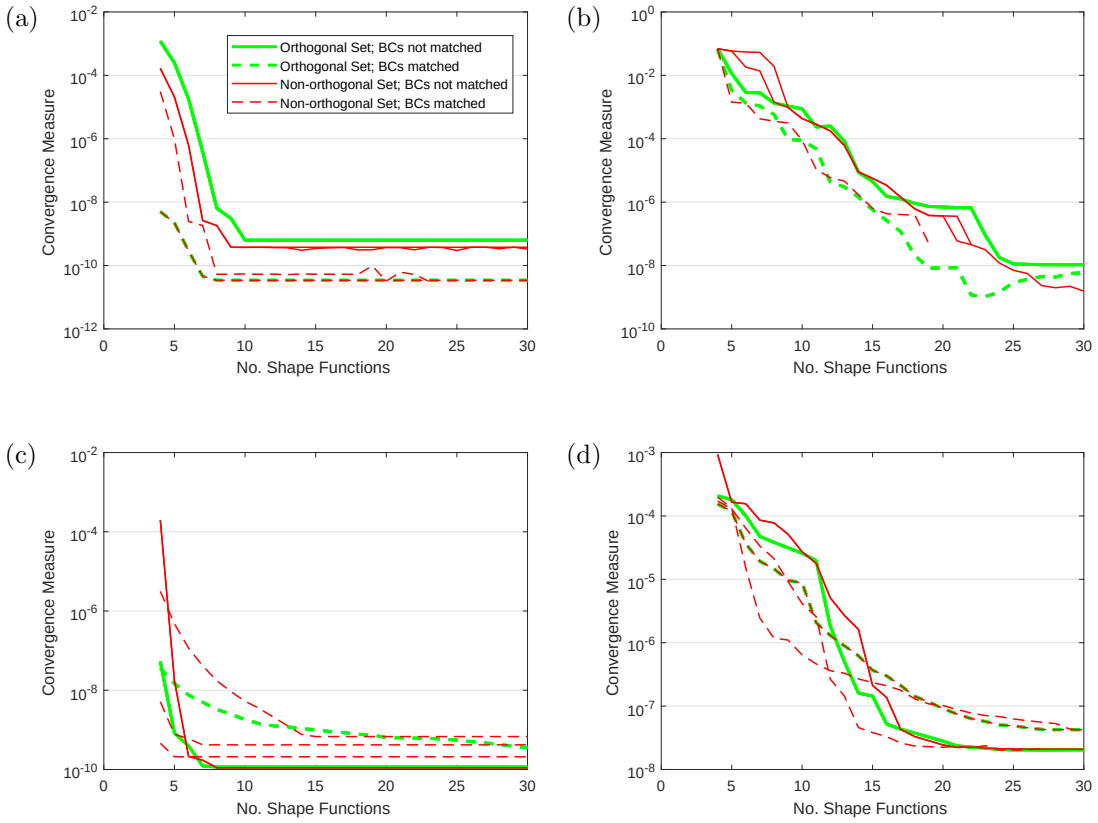

Figure 6: Variation in the convergence measure c_ν as the number of shape functions is increased. Panels (a)–(d) correspond to the load cases of figure 4, respectively.

sets a few trends may be observed; firstly, in general the satisfaction of additional load dependent boundary conditions does appear to have a small advantage in reducing the number of states required in meeting the convergence criterion. However this does not consistently translate into a reduced computational effort in solving the static problem. Secondly although there is some variation in the results, all of the shape sets offer broadly the same performance (with the exception of the outlying reverse polynomial tip global entry).

To further examine the performance of each test case the shape sets are now expanded and the change in convergence and computational complexity tracked. Figure 6 shows the convergence variation resulting from this process; note that this set expansion is achieved by systematically adding a single shape at a time to the Θ, Ψ or Φ set that gives the greatest reduction in the convergence parameter c_ν (note that for some of the shape sets it is not possible to push the system size to 30 states, see also figure 7). Each panel corresponds to the respective load cases in figure 4 and each curve relates to one of the shape sets considered. These curves are grouped according to the property of orthogonality and whether or not additional load dependent boundary constraints are satisfied — see the legend of panel (a). Looking across these plots one notes that the advantage in using orthogonal sets and in applying additional load dependent boundary constraints is not consistently evident. For example the satisfaction of the tip load constraints appears advantageous in panel (a) but prevents the highest levels of convergence in panel (c).

In figure 7 similar results are plotted, in this case tracking the change in function evaluation required to reach a solution[2]. Once again there is little distinction in either meeting or neglecting

[2]In this case, shapes are added equally across all Euler parameters from (3,3,3) to (20,20,20)

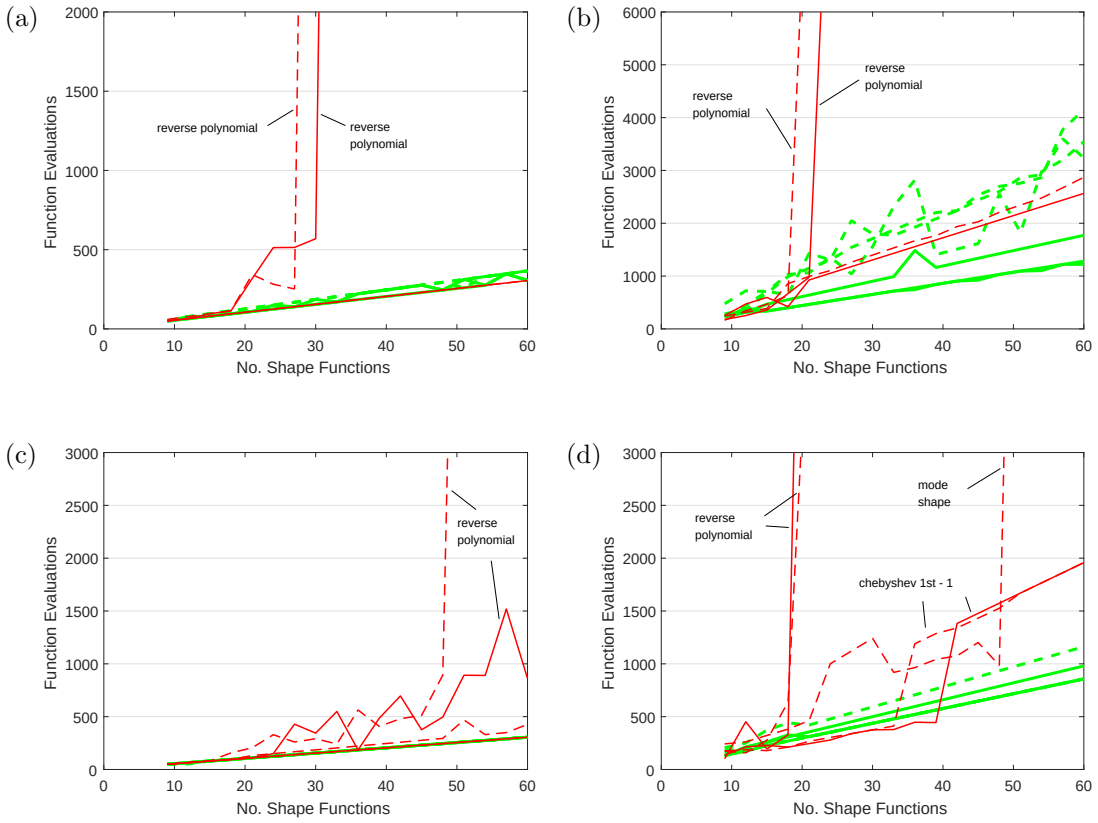

Figure 7: Variation in the number of function evaluations required to reach a static solution as the number of shape functions is increased. Panels (a)–(d) correspond to the load cases of figure 4, respectively.

the load conditions; however, certain results do clearly display a rapid blow-up in the required function evaluations as the problem size is increased. These cases are labelled in the panels to indicate the corresponding shape sets. In particular the reverse-polynomial and mode-shape sets exhibit this characteristic; the shifted 'Chebyshev 1st − 1' set also begins to deviate from the other results in panel (d). The key commonality here is that these sets alone form the non-orthogonal examples of this study. Therefore whilst the observed benefits of satisfying additional load dependent constraints is questionable, the property of orthogonality appears important in ensuring the robustness of solution when moving to particularly large shape bases.

5.1. Orthogonality

For the final part of this section the property of orthogonality is discussed in more detail. Although shape sets exhibiting this property appear to have beneficial effects on the static solution performance, it is not clear why this is the case as the system matrices for this formulation remain fully populated regardless of the properties of the shape set employed. To further investigate the property of orthogonality on the static convergence of this system consider the panels of figure 8 showing the state values for each iterate of the global (200,0,200)N tip load case — see figure 4(b); the chosen set size is $(n\theta, n\psi, n\phi) = (12, 12, 12)$. Panel (a) depicts this convergence for the orthogonal Chebyshev 1st set and panel (b), for the non-orthogonal polynomial set. For the latter case one notes that, as well as taking a greater number of iterations to solve the problem (>120), there exists a strong cross-coupling between the states wherein the variation of one state perturbs the value of the others thus hindering the smooth convergence of the entire problem.

To explore this effect, consider the residual vector $\mathbf{W}_q$ from equation (19). For the variation of each system state there corresponds a residual gradient direction $\partial \mathbf{W}_q / \partial q_n$. For a n-dimensional

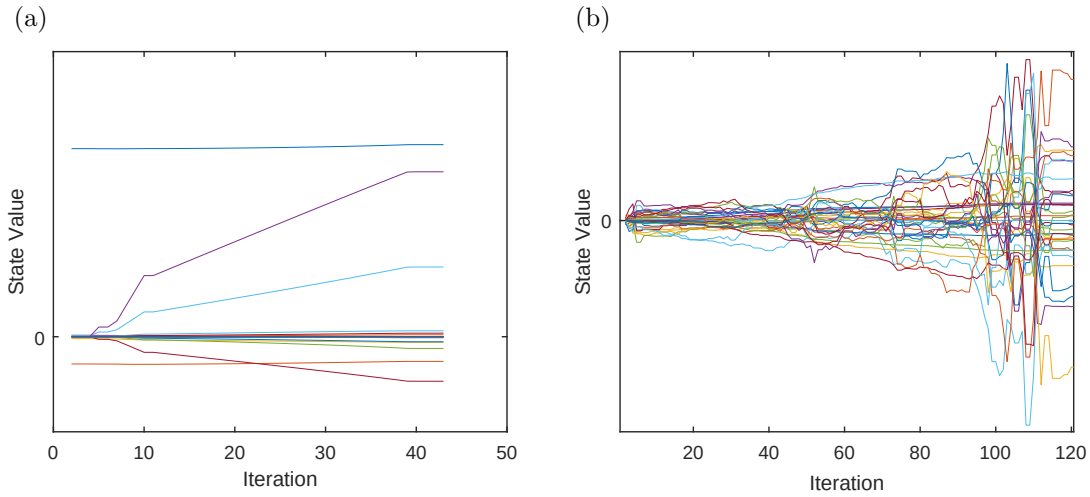

Figure 8: Convergence of (a) orthogonal Chebyshev 1st and (b) the non-orthogonal polynomial shape states for the global tip load test case.

diagonal system these n gradient directions will form an orthogonal set; i.e.

$$\frac{\partial \hat{\mathrm{W}}}{\partial q_i} \cdot \frac{\partial \hat{\mathrm{W}}}{\partial q_j} = \begin{cases} 1 & i = j \\ 0 & i \neq j \end{cases} \tag{28}$$

A visual representation of this product is presented in figure 9 for the (12,12,12) Chebyshev 1st system subject to (a) no tip load and (b) the (200,0,200) N global tip load condition; the 36×36 residual gradient combinations for this system are represented by each square element of the shaded arrays. For each square element, its color indicates the dot product magnitude (28) from dark blue = 0 to yellow = 1. For the undeformed system of panel (a) one may observe that, whilst not fully uncoupled, a diagonal band is visible that traverses this array; this coupling drops off as one moves away from this diagonal band. Looking to panel (b) one observes that this same banded structure is present, however because the Euler angle parameterisation is coupled for the generically deformed beam, this banded structure is repeated within each 12×12 subset.

Figure 10 shows the same two figures for the polynomial based system. Here, significant coupling is present within the scalar product array. For the undeformed case, the Euler parameters are uncoupled and so the off-diagonal 12×12 sub matrices are still identically zero, however the on-diagonal sub matrices are now strongly coupled with all vector products close to unity. Panel (b) reinforces this result where, due to the deformation of the structure, all sub-matrices are coupled and the entire vector product array displays strong coupling.

Hence these figures imply that a strictly orthogonal base set propagates a weaker coupling of the residual gradients of the full system, thus facilitating the efficient convergence of the static problem. Since the kinematic boundary conditions of the shape sets employed are quite generic, this orthogonality is easy to ensure in practise. Furthermore this property is readily enforcible even for more complex systems where one may wish to tailor the underlying shape sets to reflect some physical characteristics of the problem; this concept is demonstrated in the next section.

6. Wing Kink Example

Building on the previous results, we now consider a more complex geometry with discontinuity. This discontinuity is incorporated by taking the same test beam and adding a kink midway along its span; the kink is produced via a 60 degree rotation of the outer half of the undeformed beam about the global vector (0,0,-1). Note that some concepts pertaining to the treatment of discontinuity by the nonlinear beam shapes formulation were discussed in [9].

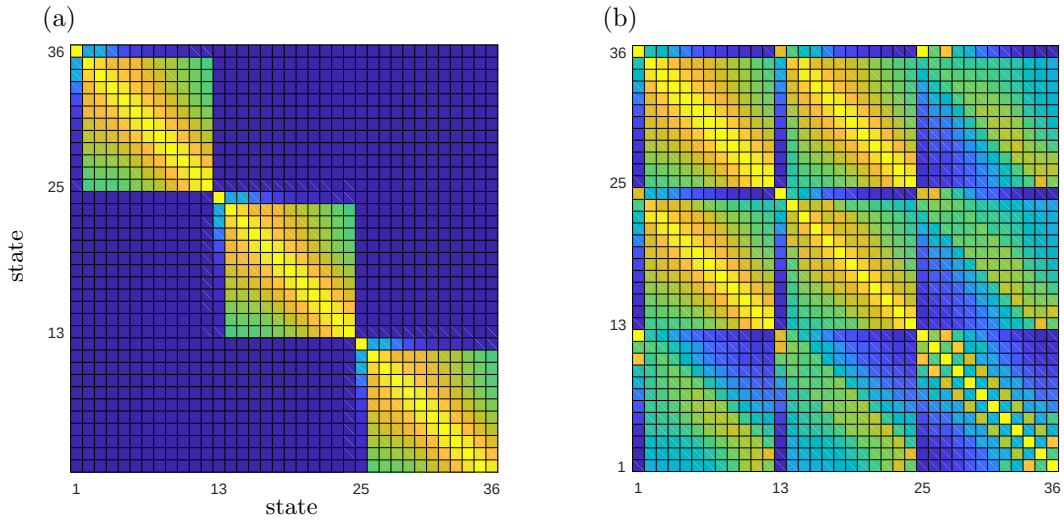

Figure 9: Residual scalar product matrix for the (12,12,12) Chebyshev system. Panel (a) corresponds to the unloaded beam, panel (b) to the global tip load case.

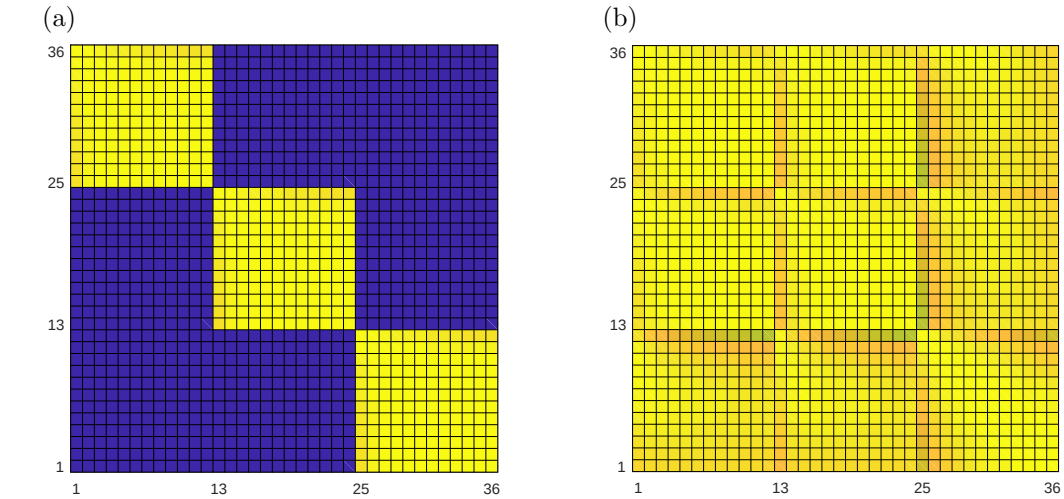

Figure 10: Residual scalar product matrix for the (12,12,12) polynomial system. Panel (a) corresponds to the unloaded beam, panel (b) to the global tip load case.

The following modifications are made to the baseline formulation. Firstly the mapping (1) is furnished with the additional discontinuous transform T_D such that

$$\begin{aligned}\mathbf{e}_{[A]} &= \boldsymbol{R}_E \begin{pmatrix} c_s\,\psi c_s\,\phi + s_n\theta s_n\psi s_n\phi & c_s\,\theta s_n\psi & c_s\,\psi s_n\phi - s_n\theta s_n\psi c_s\,\phi \\ -s_n\psi c_s\,\phi + s_n\theta c_s\,\psi s_n\phi & c_s\,\theta c_s\,\psi & -s_n\psi s_n\phi - s_n\theta c_s\,\psi c_s\,\phi \\ -c_s\,\theta s_n\phi & s_n\theta & c_s\,\theta c_s\,\phi \end{pmatrix} \boldsymbol{R}_{\boldsymbol{E}}^{\boldsymbol{T}}\,\boldsymbol{T}_D \\ &= \boldsymbol{R}_E\,\mathbf{e}_{[I]}(\theta,\psi,\phi)\boldsymbol{R}_{\boldsymbol{E}}^{\boldsymbol{T}}\,\boldsymbol{T}_D \end{aligned} \tag{29}$$

where, for the kinked geometry of this example

$$\boldsymbol{T}_D = \begin{pmatrix} \cos(\beta_{kink}) & \sin(\beta_{kink}) & 0 \\ -\sin(\beta_{kink}) & \cos(\beta_{kink}) & 0 \\ 0 & 0 & 1 \end{pmatrix} \qquad \beta_{kink} = \begin{cases} 0^\circ & s \le L/2 \\ 60^\circ & s > L/2 \end{cases} \tag{30}$$

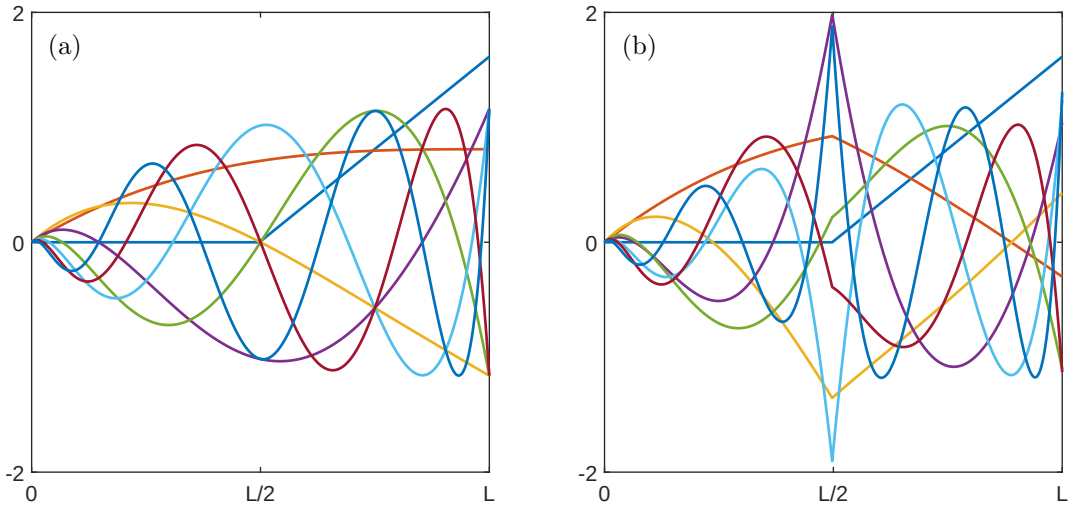

Figure 11: Modified non-smooth Chebyshev sets. Panel (a) shows the normalised Chebyshev set with appended correction function; panel (b) shows the re-orthonormalised set.

With this modification to the intrinsic system definition, the beam reference line is still obtained from the integration of $\boldsymbol{e}_{y[A]}$ as written in equation (2).

The correction term $\boldsymbol{T}_D$ is also applied to the curvature relation such that

$$\boldsymbol{\kappa}_{[A]} = \boldsymbol{T}_D^T \, \boldsymbol{R}_E \, \boldsymbol{\kappa}_{[I]} \tag{31}$$

To efficiently treat the problem one should also embed this discontinuity into the shape sets. The geometric discontinuity of this example appears as a C^1 discontinuity in the Euler basis to which the shape decomposition is applied. Hence at least one shape in the set must incorporate this discontinuity in order to reflect this characteristic in the solution of the system; a very simple correction function incorporating this feature is given by:

$$y^* = \begin{cases} 0 & s \leq L/2 \\ s - L/2 & s > L/2 \end{cases} \tag{32}$$

Appending this function to the Chebyshev 1st set and normalising with respect to the Chebyshev weighting function gives the expanded set illustrated in panel (a) of figure 11. This single modification to the shape set alongside the expanded terms of equations (29)–(31) is sufficient for the treatment of the discontinuous problem. However, at this point it is worth recalling the results of previous sections regarding the advantages of orthogonality, a property which, in the general case, is lost by the addition of an arbitrary correction function to the problem. Hence, the entire shape set is now re-orthogonalised around the new appended function using Gram-Schmidt orthonormalisation [15]. The weighting function used for this re-orthogonalisation is the scaled Chebyshev weight function $W(x)$ from the set definition (1). Furthermore, by selecting the new function (32) as the reference around which the rest of the shapes are orthogonalised, one effectively propagates the C_1 discontinuity across the entire set, further embedding this feature into the problem formulation. This effect can be seen in panel (b) of figure 11 where the resulting orthonormal shape set is depicted.

To test this modified system, the static deformation of the kinked beam subject to a 100N vertical tip load is shown in figure 12 as calculated from the modified system. The (7,5,5) Chebyshev set from figure 5 is used as the base set for this analysis; the piecewise linear correction function is

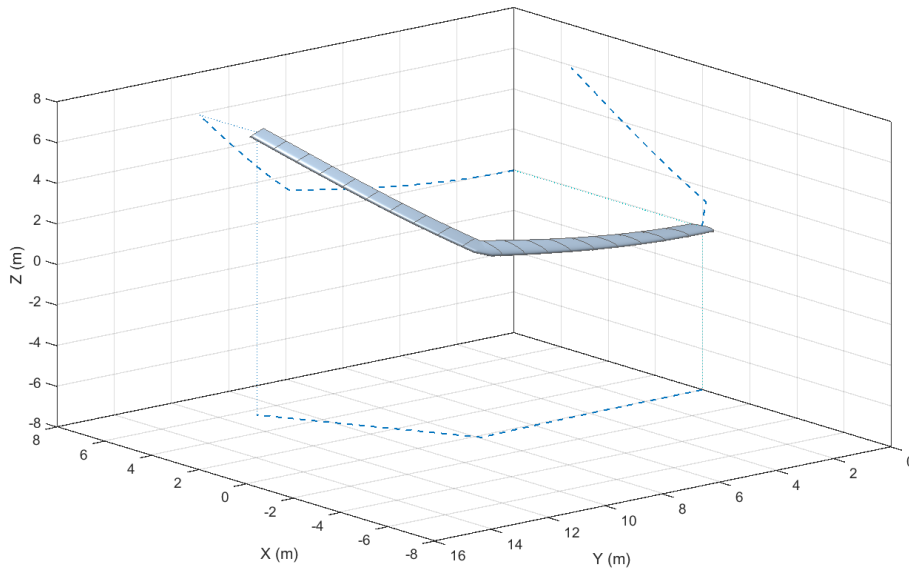

Figure 12: Static deformation of the kinked wing example subject to a global 100N vertical tip load.

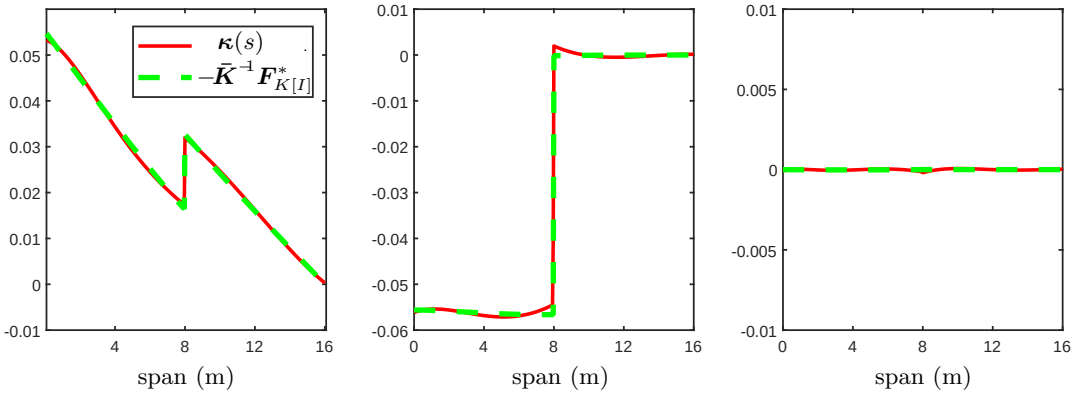

Figure 13: Depiction of the convergence criterion load balance for the discontinuous kinked wing example. The panels correspond to the balance of terms in equation (27) in the intrinsic x, y and z directions, respectively.

then appended to each Euler angle component set and re-orthogonalisation performed as depicted in figure 11. Figure 13 shows the moment-curvature balance for the predicted static deformation of this system; one sees here that the curvature profile given by the shape discretised system (red solid curves) is able to capture the midpoint discontinuity present in the internal load distribution in the intrinsic frame (green dashed curves). From visual inspection one notes that the convergence for this non-smooth case is not quite as close as that observed by the smooth results of section 12. As well as simply adding further shapes, one can also improve this convergence via the selection of a tailored correction profile; however the more sophisticated generation of these profiles is not pursued further in this study.

7. Conclusions

This study has considered the application of the nonlinear beam shapes method to the aeroelastic problem using a variety of different shape sets to approximate the span-varying kinematic variables; this was demonstrated using the Patil-Hodges half wing example. Considering the efficiency with which each shape basis represented the problem, all of the candidate sets rendered the system tractable to analysis over only a small number of describing states. In certain cases the satisfaction

of additional load dependent boundary conditions was found to yield a beneficial effect in achieving convergence. However, these benefits were slight and not observed in all test cases. Similarly the total function evaluation required in solving the static tests when using these load boundary condition was not consistently reduced.

Regarding the property of orthogonality, again the benefits were slight for moderately (and arguably realistic) sized problems. However, when moving to a much larger number of states, the orthogonal sets displayed good scalability (a roughly O(nq) scaling in the required function evaluations with nq shapes used); this was in contrast to the non-orthogonal sets which in some cases displayed a rapid blow up in computational complexity. This characteristic was rationalised by highlighting the strongly coupled nature of the algebraic equations when projected onto a non-orthogonal basis. These findings are positive from a generic problem treatment perspective. Indeed, the only real requirement is that a candidate set be orthogonal for a large problem. Since load dependent boundary conditions were found to be relatively ineffectual in improving the efficiency of static convergence, only a few kinematic constraints need be observed in practise. It was shown that these kinematic constraints are easily satisfied by any candidate set via the use of scaling transforms; furthermore, any orthogonal properties of the original function basis may be readily retained. Hence, the choice of shape functions for an arbitrary physical system is quite generic (indeed, of the orthogonal shape sets chosen for this study there was little to differentiate their performance and thus any of them constitute a suitable choice of basis). This flexibility afforded by the kinematic framework aids in the representation of more complex structural modelling problems.

The concept was demonstrated for a discontinuous system with geometric kink; the addition of an arbitrary correction function to the base shape set was used to embed the discontinuous characteristics of the structure into the admissible solution space. Orthogonality of this modified shape set was recovered by re-orthonormalising each existing shape around the added correction function. Note that one could of course treat each half of this latter discontinuous beam example as a separate smooth problem, using either an enforced boundary condition at the discontinuity or Lagrange multipliers to connect the sub-systems. However, the aim of the current development is in moving towards the modelling of complex aircraft wings with potentially numerous geometric and material discontinuities distributed along the span of the structure. In seeking a computationally efficient, low order representation, there are obvious benefits to modelling such configurations without having to subdivide the problem across every discontinuous feature. The current formulation thus provides a framework in which to embed these characteristics whilst maintaining the benefits of a geometrically nonlinear, low-order representation.

8. Acknowledgements

The research leading to these results has received funding from the InnovateUK Agile Wing Integration Project (TSB-113041). Simon Neild was supported by an EPSRC fellowship (EP/K005375/1) and Jonathan Cooper holds a Royal Academy of Engineering Research Chair.

References

[1] M. Amabili. *Nonlinear Vibrations and Stability of Shells and Plates*, chapter 15. Cambridge University Press, 2008.

[2] M. Amabili and F. Pellicano. Nonlinear Supersonic Flutter of Circular Cylindrical Shells. *AIAA Journal*, 39(4):564–573, 2001. (doi:10.2514/2.1365).

[3] M. Amabili and F. Pellicano. Multimode Approach to Nonlinear Supersonic Flutter of Imperfect Circular Cylindrical Shells. *Journal of Applied Mechanics*, 69(2):117–129, 2002. (doi:10.1115/1.1435366).

[4] T. Belytschko and L. W. Glaum. Applications of Higher Order Corotational Stretch Theories to Nonlinear Finite Element Analysis. *Computers & Structures*, 10(1):175–182, 1979. (doi:10.1016/0045-7949(79)90085-3).

[5] T. Belytschko and B. J. Hsieh. Nonlinear Transient Finite Element Analysis with Convected Coordinates. *International Journal for Numerical Methods in Engineering*, 7(3):255–271, 1973. (doi:10.1002/nme.1620070304).

[6] C. E. S. Cesnik and E. L. Brown. Modeling of High Aspect Ratio Active Flexible Wings for Roll Control. In *43rd AIAA/ASME/ASCE/AHS/ASC Structures, Structural Dynamics, and Materials Conference*, Denver, Colorado, 2002. AIAA.

[7] A. J. Eaton, C. Howcroft, E. B. Coetzee, S. A. Neild, M. H. Lowenberg, and J. E. Cooper. Numerical Continuation of Limit Cycle Oscillations and Bifurcations in High-Aspect-Ratio Wings. *Aerospace*, 5(3), 2018. (doi:10.3390/aerospace5030078).

[8] D. H. Hodges. A Mixed Variational Formulation Based on Exact Intrinsic Equations or Dynamics of Moving Beams. *International Journal of Solids and Structures*, 26(11):1253–1273, 1990. (doi:10.1016/0020-7683(90)90060-9).

[9] C. Howcroft, R. G. Cook, S. A. Neild, M. H. Lowenberg, J. E. Cooper, and E. B. Coetzee. On the geometrically exact low-order modelling of a flexible beam: formulation and numerical tests. *Proc. R. Soc. A*, 474(2216), 2018. (doi:10.1098/rspa.2018.0423).

[10] J. Katz and A. Plotkin. *Low-Speed Aerodynamics*, chapter 8. Cambridge University Press, 2nd edition, 2001.

[11] D. I. Manolas, V. A. Riziotis, and S. G. Voutsinas. Assessing the Importance of Geometric Nonlinear Effects in the Prediction of Wind Turbine Blade Loads. *Journal of Computational and Nonlinear Dynamics*, 10(4), 2015. (doi:10.1115/1.4027684).

[12] M. J. Patil and D. H. Hodges. Limit-Cycle Oscillations in High-Aspect-Ratio Wings. *Journal of Fluids and Structures*, 15:107–132, 2001. (doi:10.1006/jfls.2000.0329).

[13] M. J. Patil, D. H. Hodges, and C. E. S. Cesnik. Nonlinear Aeroelasticity and Flight Dynamics of High-Altitude Long-Endurance Aircraft. *Journal of Aircraft*, 38(1):88–94, 2001. (doi:10.2514/2.2738).

[14] M. Powell. A Fortran Subroutine for Solving Systems of Nonlinear Algebraic Equations. In P. Rabinowitz, editor, *Numerical Methods for Nonlinear Algebraic Equations*. 1970.

[15] E. Schmidt. Zur Theorie der linearen und nichtlinearen Integralgleichungen. *Mathematische Annalen*, 63(4):433—-476, 1907.

[16] A. A. Shabana, H. A. Hussien, and J. L. Escalona. Application of the Absolute Nodal Coordinate Formulation to Large Rotation and Large Deformation Problems. *Journal of Mechanical Design*, 120(2):188–195, 1998. (doi:10.1115/1.2826958).

[17] J. C. Simo and L. Vu-Quoc. A Finite Strain Beam Formulation. The Three-Dimensional Dynamic Problem. Part I. *Computer Methods in Applied Mechanics and Engineering*, 49:55–70, 1985. (doi:10.1016/0045-7825(85)90050-7).

[18] J. C. Simo and L. Vu-Quoc. A Three-Dimensional Finite-Strain Rod Model. Part II: Computational Aspects. *Computer Methods in Applied Mechanics and Engineering*, 58:76–116, 1986. (doi:10.1016/0045-7825(86)90079-4).

[19] W. Su and C. E. S. Cesnik. Strain-based geometrically nonlinear beam formulation for modeling very flexible aircraft. *International Journal of Solids and Structures*, 48:2349–2360, 2011. (doi:10.1016/j.ijsolstr.2011.04.012).

[20] D. Tang and E. H. Dowell. Experimental and Theoretical Study on Aeroelastic Response of High-Aspect-Ratio Wings. *AIAA Journal*, 39(8):1430–1441, 2001. (doi:10.2514/2.1484).